Acta Oceanol. Sin., 2020, Vol. 39, No. 11, P. 69–81
https://doi.org/10.1007/s13131-020-1676-z
http://www.hyxb.org.cn
E-mail: hyxbe@263.net

Spatial structure of turbulent mixing of an anticyclonic mesoscale eddy in the northern South China Sea

Yongfeng Qi[1†], Chenjing Shang[2†], Huabin Mao[1, 3*], Chunhua Qiu[4], Changrong Liang[1], Linghui Yu[1], Jiancheng Yu[5], Xiaodong Shang[1]

[1] State Key Laboratory of Tropical Oceanography, South China Sea Institute of Oceanology, Chinese Academy of Sciences, Guangzhou 510301, China

[2] Shenzhen Key Laboratory of Marine Bioresources and Eco-environmental Science, College of Life Science and Oceanography, Shenzhen University, Shenzhen 518060, China

[3] Ocean College, Zhejiang University, Zhoushan 316021, China

[4] The Center for Coastal Ocean Science and Technology, School of Marine Sciences, Sun Yat-sen University, Guangzhou 510275, China

[5] State Key Laboratory of Robotics, Shenyang Institute of Automation, Chinese Academy of Sciences, Shenyang 110016, China

Received 23 June 2020; accepted 10 August 2020

Abstract

Upper turbulent mixing in the interior and surrounding areas of an anticyclonic eddy in the northern South China Sea (SCS) was estimated from underwater glider data (May 2015) in the present study, using the Gregg-Henyey-Polzin parameterization and the Thorpe-scale method. The observations revealed a clear asymmetrical spatial pattern of turbulent mixing in the anticyclonic eddy area. Enhanced diffusivity (in the order of 10^{-3} m^2/s) was found at the posterior edge of the anticyclonic mesoscale eddy; on the anterior side, diffusivity was one order of magnitude lower on average. This asymmetrical pattern was highly correlated with the eddy kinetic energy. Higher shear variance on the posterior side, which is conducive to the triggering of shear instability, may be the main mechanism for the elevated diffusivity. In addition, the generation and growth of sub-mesoscale motions that are fed by mesoscale eddies on their posterior side may also promote the occurrence of strong mixing in the studied region. The results of this study help improve our knowledge regarding turbulent mixing in the northern SCS.

Key words: mesoscale eddy, turbulent mixing, South China Sea, GHP parameterization, Thorpe-scale method

Citation: Qi Yongfeng, Shang Chenjing, Mao Huabin, Qiu Chunhua, Liang Changrong, Yu Linghui, Yu Jiancheng, Shang Xiaodong. 2020. Spatial structure of turbulent mixing of an anticyclonic mesoscale eddy in the northern South China Sea. Acta Oceanologica Sinica, 39(11): 69–81, doi: 10.1007/s13131-020-1676-z

1 Introduction

The South China Sea (SCS) is the largest semi-enclosed marginal sea in the northwestern Pacific Ocean. Its large-scale currents are driven by the East Asian monsoon (Xie et al., 2003). It has been reported that the SCS experiences a range of multiscale dynamical processes including wind- and density-driven circulation (Qu, 2000; Wang et al., 2011), strong internal waves (Alford et al., 2015; Huang et al., 2016), enhanced turbulent mixing (Tian et al., 2009; Liang et al., 2017), and energetic mesoscale eddies (Wang et al., 2003; Zhang et al., 2013; Qiu et al., 2019b). Among these processes, mesoscale eddies with strong kinetic energies play an important role in the dynamics across a range of scales (Chelton et al., 2011) and are a key transport mechanism of oceanic material (Zhang et al., 2014).

Mesoscale eddies in the northern SCS have received much attention in the past few decades, which is evident in both hydrographic datasets and satellite sea-level anomaly data (Li et al., 1998; Li and Pohlmann, 2002; Yuan et al., 2007; Chow et al., 2008; Wang et al., 2003, 2008; Chen et al., 2011; Chu et al., 2014; Zhang et al., 2016; Qiu et al., 2019b). Previous studies have examined eddy structures, eddy life-cycles (in terms of their origination, shifts, development, and decay), and the associated transport of energy and matter in the northern SCS (Wang et al., 2005; Nan et al., 2015; Zhang et al., 2016; Zheng et al., 2017; Qiu et al., 2019a). The prevailing dynamical paradigm is that the oceanic eddies are

Foundation item: The National Key R&D Plan of China under contract Nos 2017YFC0305904, 2017YFC0305804 and 2016YFC1401404; the National Natural Science Foundation of China under contract Nos 41876023, 41630970, 41806037, 41706137 and 41806033; the Guangdong Science and Technology Project under contract Nos 2019A1515111044, 2018A0303130047 and 2017A030310332; the Guangzhou Science and Technology Project under contract No. 201707020037; the Natural Science Foundation of Shenzhen University under contract No. 2019078; the Dedicated Fund for Promoting High-quality Economic Development in Guangdong Province (Marine Economic Development Project) under contract No. GDOE[2019]A03; the Independent Research Project Program of State Key Laboratory of Tropical Oceanography under contract Nos LTOZZ1902 and LTO1909.
*Corresponding author, E-mail: maohuabin@scsio.ac.cn
†These authors contributed equally to this work.

generated through the hydrodynamic instabilities of ocean currents with the release of available potential and kinetic energy built up by large-scale wind and surface buoyancy fluxes (Gill et al., 1974; Ferrari and Wunsch, 2009).

The formation of mesoscale eddies in the SCS occurs mainly through shedding from the Kuroshio intrusion and its instability (Li et al., 1998; Jia et al., 2004; Yuan et al., 2006; Zhang et al., 2017) and the action of the local wind-stress jet (Wang et al., 2008). Eddies from the Luzon Strait usually follow one of three tracks, namely southwestward to Hainan Island, westward into the 1 000-m isobath, or southward (Nan et al., 2011b). A proportion of eddies can drift southwestward along the continental slope for more than a thousand kilometers and last for several months after their formation from a Kuroshio intrusion (Chen et al., 2011; Nan et al., 2011b; He et al., 2018). During their propagation, the mesoscale eddies can modulate basin-scale circulation (Yang and Liu, 2003), affecting small-scale internal waves (Xie et al., 2015), inducing cross-shelf flow (Wang et al., 2018), and evoking sub-mesoscale motions (Zhang et al., 2016).

In addition to the mesoscale eddy processes, turbulent mixing in the northern SCS has received much attention in the last twenty years. The northern SCS is a hotspot of turbulent mixing (St. Laurent, 2008); it is reported that the turbulent mixing rates in the north SCS can be two orders of magnitude higher than that in the Pacific Ocean (Tian et al., 2009; Klymak et al., 2011). The elevated turbulent mixing in the SCS drives water exchange between the SCS and the Pacific (Zhou et al., 2014), and plays a key role in driving the SCS circulation (Qu et al., 2006). The breaking of internal waves (i.e., internal solitary waves, internal tides, and near-inertial internal waves) is considered the dominant factor driving the high-level mixing in the northern SCS (Yang et al., 2016; Bai et al., 2019). Most of those previous studies focusing on turbulent mixing in the SCS were based on large distance station measurements with scales reach dozens of kilometers. However, with low spatial measurements, it is difficult to depict spatial characteristics of mesoscale motions (such as mesoscale eddies) mixing.

Much attention has been paid to mesoscale eddies and turbulent mixing individually. However, the influence of the mesoscale eddies on the turbulent mixing in the SCS has only recently received attention. Several mechanisms of turbulent mixing influenced by mesoscale eddies have been reported. Anticyclonic and cyclonic eddies have different effects on turbulent mixing in the north SCS, with the former strengthening mixing and latter weakening mixing, respectively (Yang et al., 2014). Potential causes of the enhanced mixing within the anticyclonic eddies include the breaking of strong internal tides radiating from the Luzon Strait and the breaking of near-inertial waves radiating from the eddy itself (Zhang et al., 2016), the eddy reinforced down-propagation of near-inertial waves (Yang et al., 2014), the near-inertial waves generated by the interaction of mesoscale eddies, and unique bottom topography (Sun et al., 2016). Recently, Yang et al. (2017) found that several times more turbulent mixing occurred in the surface mixed layer of the periphery of anticyclonic eddies compared to that in the eddy center. The more energized sub-mesocale motions in the periphery were a key factor leading to the spatial feature of mixing. The mesoscale eddies in the SCS can dissipate effectively over complex rough topography, and the generation of sub-mesoscale motions and lee waves are two pathways for the transfer of mesoscale eddy energy down to small dissipation scales (Yang et al., 2019).

Although some researchers have studied the influence of mesoscale eddy on turbulent mixing in the SCS, more observations, especially high spatial resolution observations, are needed to examine the spatial structure of turbulent mixing of mesoscale eddy to identify the effects of the physical processes such as sub-mesoscale eddy. Here, based on the glider measurement results obtained in May 2015, we present an assessment of the spatial structure in high spatial resolution, less than 4 km of turbulent mixing within and surrounding an anticyclonic eddy in the northern SCS.

2 Data and methods

2.1 *Data*

The primary data source was a Chinese underwater glider (Sea-Wing) deployed in the northern SCS (Fig. 1a). The glider passed through the center of an anticyclonic mesoscale eddy on May 18, 2015. The glider was released at 21°N, 119°E on April 1, 2015, traveled southwestward for more than 700 km, and was finally retrieved at 18°N, 114°E on June 1, 2015 (indicated by the black line in Fig. 1a). Temperature, salinity, and pressure were measured by a Seabird CTD installed on the glider. The glider profiled the water column to a depth of 1 000 m and captured 205 vertical temperature and salinity profiles.

To examine the surface characteristics of the studied anticyclonic eddy, satellite altimeter-based sea level anomaly (SLA) and absolute dynamic topography (ADT) data distributed by the Copernicus Marine Environment Monitoring Service (CMEMS, http://marine.copernicus.eu) were obtained. The SLA dataset merged observations from different altimetry satellites (Jason-3, Sentinel-3A, HY-2A, Saral/AltiKa, Cryosat-2, Jason-2, Jason-1, T/P, ENVISAT, GFO, and ERS1/2), and geophysically and meteorologically corrected for tides, ionospheric effects, and atmospheric pressure with gridded spatial and temporal resolutions of (1/4)° and one day, respectively. The SLA data represent the differences between ADT and mean dynamic topography (MDT). The specific product used was SEALEVEL_GLO_PHY_L4_REP_OBSERVATIONS_008_047, and a full description of the dataset is available at http://cmems-resources.cls.fr/documents/PUM/CMEMS-SL-PUM-008-032-051.pdf.

The global (1/12)° reanalysis product of the Hybrid Coordinate Ocean Model (HYCOM) was used to investigate the surface velocity accompanying the mesoscale eddy (Section 4), which is available at http://hycom.org/dataserver/glb-reanalysis. This product assimilates multiple observational datasets, including satellite altimeter and sea-surface temperature (SST) data and *in-situ T-S* profiles from different instruments (e.g., CTDs, XBTs, and Argo floats). The HYCOM simulations had 40 vertical layers with daily archives and included three-dimensional velocity and *T-S* fields. It was previously reported that the HYCOM product performed well in simulating eddies in the northern SCS (Park and Famer, 2013; Zhang et al., 2017).

The Aviso eddy atlas was adopted to display the variation in the physical fields of the eddy (https://www.aviso.altimetry.fr). This dataset contains a range of physical data, including eddy radius, eddy amplitude, and eddy rotation speed. The data-processing method for this dataset is described in detail by Chelton et al. (2011).

Historical temperature and salinity data from the Argo dataset (http://argo.ucsd.edu) were also utilized to identify the origin of the eddy. Sea surface wind data from a blended wind dataset (Zhang et al., 2006) was used to exclude the effect of surface wind fields on mixing. The blended wind data combined multiple

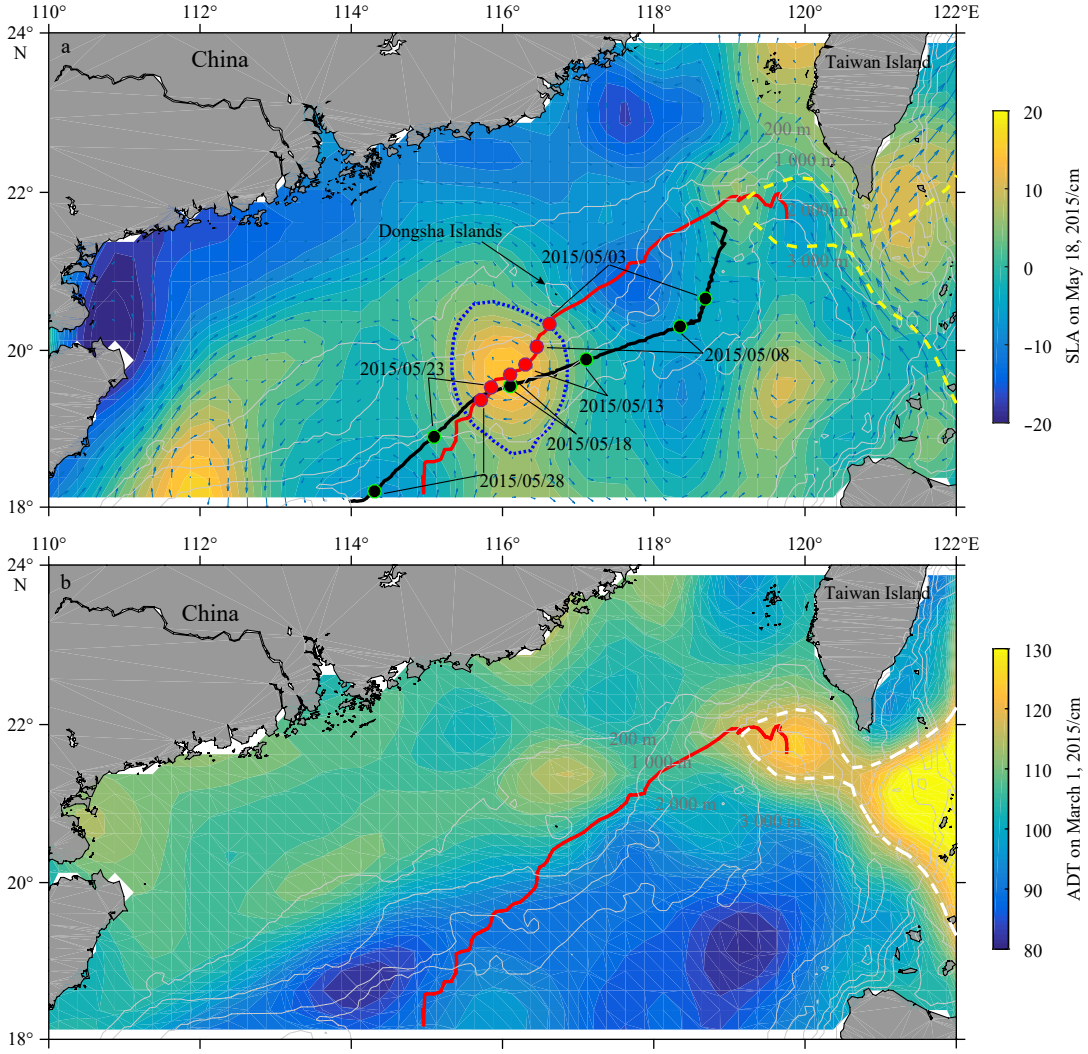

Fig. 1. Trajectories of the anticyclonic eddy and underwater glider. a. Sea level anomaly (SLA) data for May 18, 2015. The red line indicates the track of the studied anticyclonic eddy. The black line shows the track of the underwater glider. The studied anticyclonic eddy is marked with a blue dashed line. The locations of the eddy center and glider on May 3, May 8, May 13, May 18, May 23, and May 28 are indicated. b. Absolute dynamic topography (ADT) on March 1, 2015. The red line indicates the track of the studied anticyclonic eddy. The yellow dash line in a and white dash line in b show an ADT of 118 cm. Bathymetry of the South China Sea with the 200 m, 1 000 m, 2 000 m and 3 000 m isobaths overlaid in a and b.

satellite observations and were used to fill any data gaps in both time and space (http://www.ncdc.noaa.gov/data-access/marineocean-data/blended-global/blended-sea-winds).

2.2 *Gregg-Henyey-Polzin parameterization*

The Gregg-Henyey-Polzin (GHP) parameterization is one of the most widely used methods of quantifying ocean turbulence from CTD measurements (Gregg et al., 2003; Kunze et al., 2006). The GHP scaling based on internal wave-wave interaction theory and was first developed by Henyey et al. (1986). We employed the GHP parameterization to qualify the diapycnal diffusivities from CTD measurements installed on the glider. The GHP is expressed as follows:

$$K_\rho = K_0 \frac{\langle \zeta_z^2 \rangle^2}{{}_{\mathrm{GM}}\langle \zeta_z^2 \rangle^2} h(R_w) j\left(\frac{f}{N}\right), \tag{1}$$

$$h(R_w) = \frac{1}{6\sqrt{2}} \frac{R_w(R_w+1)}{\sqrt{R_w-1}}, \tag{2}$$

and

$$j\left(\frac{f}{N}\right) = \frac{f \operatorname{arccosh}(N/f)}{f_{30} \operatorname{arccosh}(N/f)}, \tag{3}$$

where K_0=5×10^{-6} m^2/s, $\langle \zeta_z^2 \rangle$ represents the fine-scale internal wave strain variance inferred from observations, and ${}_{\mathrm{GM}}\langle \zeta_z^2 \rangle$ is the strain variance inferred from the Garrett and Munk (GM) spectrum (Garrett and Munk, 1972, 1975). In the GM model, an open-ocean internal wave-field was assumed at a fixed buoyancy frequency (N_0=5.2×10^{-3} s^{-1}) at the latitude of 30°. The functions f and N are the Coriolis and buoyancy frequencies, respectively, and R_w is the shear/strain variance ratio, which was set to 7 as suggested by Kunze et al. (2006) and used by Yang et al. (2016) to quantify the mixing in the SCS. To quantify strain $\langle \zeta_z^2 \rangle$, the glider

profiles were first separated into half-overlapping 300-m-long segments, starting from the bottom and excluding the data in the surface mixed layer. The internal wave strain was estimated from the buoyancy frequency $\xi_z=(N^2-\overline{N^2})/\overline{N^2}$, where $\overline{N^2}$ is the mean value based on quadratic fitting to each buoyancy frequency segment. Strain variance was obtained as $\left\langle \xi_z^2 \right\rangle = \int_{\min(k_z)}^{\max(k_z)} S\left[\xi_z\right](k_z)\,\mathrm{d}k_z$. For strain variance integration, the minimum integrated wavenumber was set to 0.042 rad/m corresponding to a vertical wavelength λ_z=150 m. This was chosen as a lower wavenumber might be influenced by strong background stratification in the pycnocline (Kunze et al., 2006; Jing and Wu, 2013). The upper bound is set to 0.419 rad/m, corresponding to vertical wavelength λ_z=15 m. The GM strain variance was computed over the same wavenumber band as follows:

$$_{\mathrm{GM}}\left\langle \xi_z^2 \right\rangle = \frac{\pi E_0 b j_*}{2} \int_{\min(k_z)}^{\max(k_z)} \frac{k^2}{(k+k_*)}\mathrm{d}k_z, \tag{4}$$

where E_0=6.3×10^{-5} is the dimensionless energy level; b=1 300 m, which the scale depth of the thermocline; j_*=3, which is the reference mode number; and $k_*=(\pi j_* N)/(bN_0)$, which is the reference wavenumber.

The GHP scaling was initially developed for the open ocean, and its applicability in the marginal sea should be further examined due to its potential limitations (Polzin et al., 2014). To improve the reliability of results, we also used the Thorpe-scale method to estimate the diffusivity.

2.3 *Thorpe-scale method*

Based on the well-established relationship between the Ozmidov scale ($L_O=\sqrt{\varepsilon/N^3}$, where ε is the dissipation rate) and the Thorpe scale (L_T; Dillon, 1982), and the Osborn's relationship between the dissipation rate and diapycnal diffusivity ($K_\rho=\Gamma\varepsilon/N^2$, where Γ is the mixing efficiency and is selected as 0.2) (Osborn, 1980), the diapycnal diffusivity can be related to L_T as follows:

$$K_\rho = 0.64\Gamma L_T^2 N, \tag{5}$$

where L_T can be calculated as the RMS displacement of a parcel, and the buoyancy frequency N is evaluated using the gradient of the reordered density profile. Here, the displacement is defined as the depth difference between a measured potential temperature profile and its reordered version (Mater et al., 2015). In this study, we applied this method to estimate the diffusivity and compared with the GHP results to improve the reliability of the results.

3 Results

3.1 *Water mass characteristics of the anticyclonic eddy and its origin*

The glider well transited the center of the eddy (Fig. 1). To

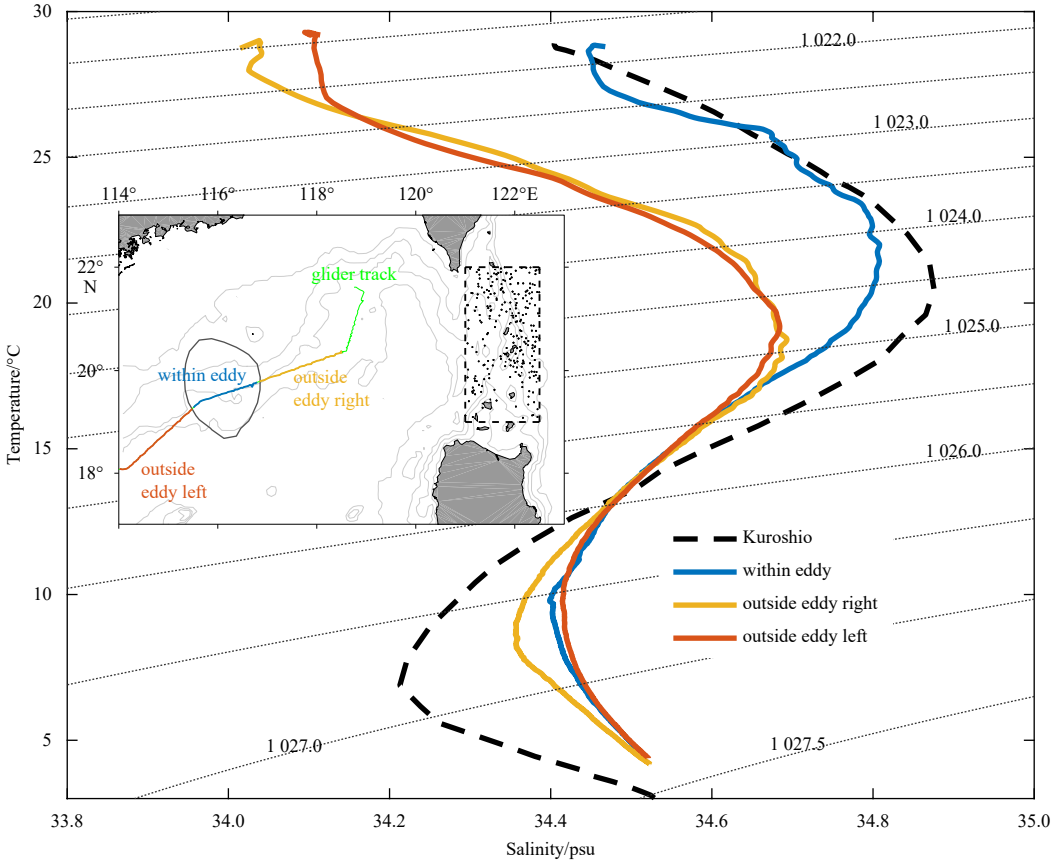

Fig. 2. Mean *T*-*S* diagrams of water masses within and outside of the studied eddy (with the potential density of σ_θ in kg/m^3 contours overlaid). The blue, red, and yellow lines show data for the water forming the within eddy (115.5°–117°E), outside eddy left (114°–115.5°E), and outside eddy right (117°–118.5°E) sections, respectively. The black dashed line shows data for the Kuroshio Current water based on historical Argo *T*-*S* profiles within the black boxes of the inset figure.

identify the origin of the anticyclonic eddy, historical temperature and salinity data obtained from Argo data center for the Kuroshio Current in the western Pacific (19°–22°N, 121°–122.5°E) were compared with the *in-situ T/S* data. The historical profile of the Kuroshio Current was derived by averaging 654 data profiles. First, we separated the observed glider data into the following three categories (Fig. 2): (1) region within the eddy (115.5°–117°E); (2) left region outside the eddy (114°–115.5°E), and (3) right region outside the eddy (117°–118.5°E). The outside eddy left region corresponded to the anterior area of the eddy movement, and the outside eddy right region corresponded to the posterior area of the eddy. When comparing the water mass characteristics within the three regions, a notable feature is that the upper-layer water within the eddy region differed from that in the outside eddy (both left and right) regions, indicating different water genesis mechanisms.

The *T-S* characteristics in each region of the eddy were then compared with the Kuroshio Current (Fig. 2). For the Kuroshio Current, the *T-S* curve showed a reversed "S" shape, indicating that the water was warmer and saltier in the upper layer (<300 m) but colder and fresher in the intermediate layer (300–1 000 m); the upper-layer salinity maximum and intermediate-layer salinity minimum reached 34.87 psu and 34.22 psu, respectively. For the north SCS water recorded by glider (the outside eddy left and right regions, water was cooler and fresher in the upper layer but warmer and salter in the intermediate layer; water in the upper-layer salinity maximum and intermediate-layer salinity minimum reached 34.68 psu and 34.26 psu, respectively. Based on their similar water mass characteristics, the upper-layer water in the anticyclonic eddy probably originated from the Kuroshio Current.

To confirm the origin of the eddy, the movement track was derived from the SLA and ADT datasets. Following the identification criteria and tracking algorithm proposed by Chelton et al. (2011), the track of the studied eddy is shown in Fig. 1b; the eddy emerged southwest of Taiwan Island, after its formation, rotated in the nearby area for approximately one month before drifting southwestward along the continental slope. The similar water mass characteristics of the eddy and the Kuroshio Current water indicates that there was no notable exchange between the eddy and the northern SCS water during its southwestward movement, although the traveled distance encompassed four latitudes and passed the complex bottom topography of the Dongsha Islands area (Fig. 1).

Before its formation, the ADT map shows that the eddy was shedding from the Kuroshio intrusion. Figure 1b shows the ADT for the Luzon Strait on March 1, 2015. The white line indicates an ADT of 118 cm, indicating that the eddy originated from the Kuroshio Current. The shading of the Kuroshio intrusion has also been observed by other scientists (Caruso et al., 2006; Jia and Chassignet, 2011; Nan et al., 2011a; Hu et al., 2012; Guo et al., 2013; Zhang et al., 2017). Recently, Zhang et al. (2017) reported that the barotropic instability of the Kuroshio Loop Current constitutes the primary generation mechanism for eddy shedding from the Kuroshio Current to the northern SCS.

3.2 *Variation of the physical field of the anticyclonic eddy*

The eddy was continuously weakening as it moved in southwest direction. Based on the physical field data (Aviso eddy atlas data) for the period between May 3 and May 18 (Fig. 3), the radius of the eddy decreased by half from 140 km to 70 km, with the time of strength change was during May 12 and May 14. The eddy rotational speed decreased from 32 cm/s on May 3 to 27.2 cm/s on May 13 and then increased to approximately 29.2 cm/s on

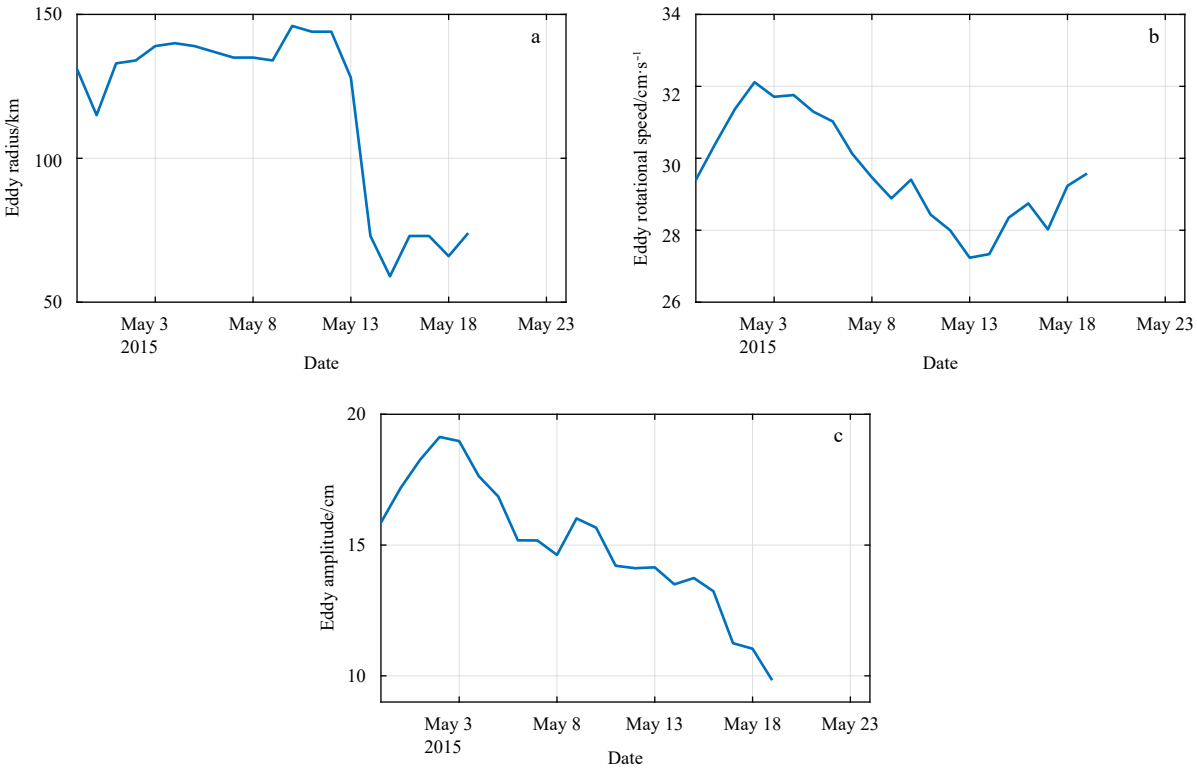

Fig. 3. Variations in the physical field of the studied anticyclonic eddy, including the eddy radius (a), rotational speed (b), and amplitude (c).

May 18. At the same time, the amplitude of the eddy decreased from 19 cm on May 3 to 11 cm on 18 May. These physical field variations indicate that both the kinetic energy and potential energy of the eddy were weakening during this period. Energy dissipation is one of the main mechanisms driving variation of the physical field characteristics of eddies (Zhang et al., 2016). In addition, here we focus on mixing processes and the diffusivity of the eddy (Section 3.4).

3.3 *Structure of the anticyclonic eddy*

Matching the underwater glider tracks with the SLA satellite data, the glider cut through the eddy between May 13 and May 23, 2015 (Fig. 1). On May 18, the anticyclonic eddy entered the region 19.72°N, 116.13°E, when it had a radius (R) of approximately 137 km (Fig. 1a). Vertical profiles of potential temperature, salinity, potential density, and the baroclinic geostrophic velocities along the glider track are shown in Fig. 4. Here, the baroclinic geostrophic current v_g at depth of z was calculated from the thermal wind relationship (Qiu et al., 2019b) that, $v_{\text{g-glider}}=v_0-\frac{g}{f\rho_0}\int_{z_0}^{z}\frac{\partial\rho_z}{\partial s}\mathrm{d}z$, $v_g=\frac{v_{\text{g-glider}}}{\cos\alpha}$, where $v_{\text{g-glider}}$ is the geostrophic velocity perpendicular to the glider path, α is angle between the glider path and the line between the location of glider and eddy centre, ρ_0 is the reference density (1 025 kg/m^3), ρ is the potential density of seawater, and f is the local Coriolis parameter. As such, the geostrophic velocities were obtained by integrating the thermal wind relationship from a reference depth (z_0) to the calculation depth (z). The reference depth (z_0) was set to 1 000 m, where velocity v_0 was assumed to be zero.

These calculations showed that a trough existed in the contours of temperature, salinity, and potential density; depressed contours were notable between 100 m and 300 m, with the depressed center being consistent with the position of the altimeter-derived eddy center (the white dashed line in Fig. 4). This indicates that the altimeter-derived location of the eddy center was reliable. The vertical profiles of salinity display a salty region between 100 m and 200 m, where salinity ⩾34.8 psu (Fig. 4b), which is similar to the Kuroshio Current waters (Qu, 2000). The salty water originated from the Kuroshio Current, with Hu et al. (2012) pointing out that anticyclonic eddies carry high-salinity subsurface waters from the Northwest Pacific into the northern SCS (Fig. 2). The vertical distribution of baroclinic geostrophic velocities is shown in Fig. 4d. To the left of the eddy center, the velocity was positive; to the right, it was negative. The velocity increased in magnitude from the eddy center and reached its maximum of approximately –0.8 m/s at 117°E and 0.8 m/s at 115.3°E. The location of maximum velocity corresponded to the edge of the anticyclonic eddy; outside of the eddy edge, velocities began to drop. The depth where the geostrophic speeds were above 20 cm/s almost reached 600 m.

In the northern South China Sea, it has been confirmed that axis of mesoscale eddies strongly tilts southwestward from surface to bottom (Zhang et al., 2016). The tilting distance reached up to ~100 km for both anticyclonic eddy and cyclonic eddy from surface to the depth of 2 000 m. This study also displayed a tilt feature. A notable feature was that the tilt of geostrophic velocities (Fig. 4d). In the centre of the eddy, the zero geostrophic velocities tilt westward around 0.3 degree of longitude from surface to 1 000 m, which was consistent with the study reported by Zhang et al. (2016).

3.4 *Diapycnal diffusivities*

3.4.1 *GHP parameterization results*

A section of inferred diffusivity (K_ρ) based on the GHP scaling is shown in Fig. 5. The diffusivity values ranged from a minimum of less than 10^{-5} m^2/s to a maximum of >$10^{-2.5}$ m^2/s, which indicates marked asymmetry. High-level mixing and diffusivity

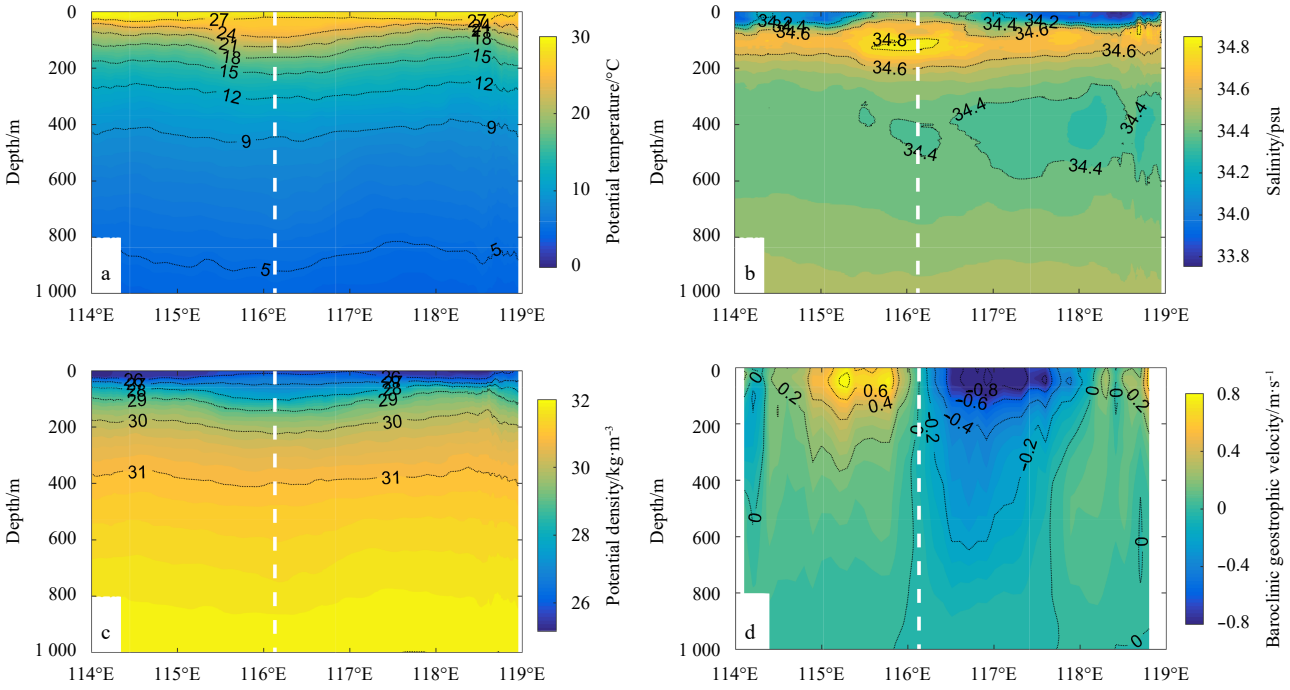

Fig. 4. Vertical profiles of physical fields of the eddy. Potential temperature (a), salinity (b), potential density along the glider track (c), and baroclinic geostrophic velocity across the track (d). The white dashed lines indicate the eddy center derived from SLA data. The positive and negative values in d represent northward and southward velocities, respectively.

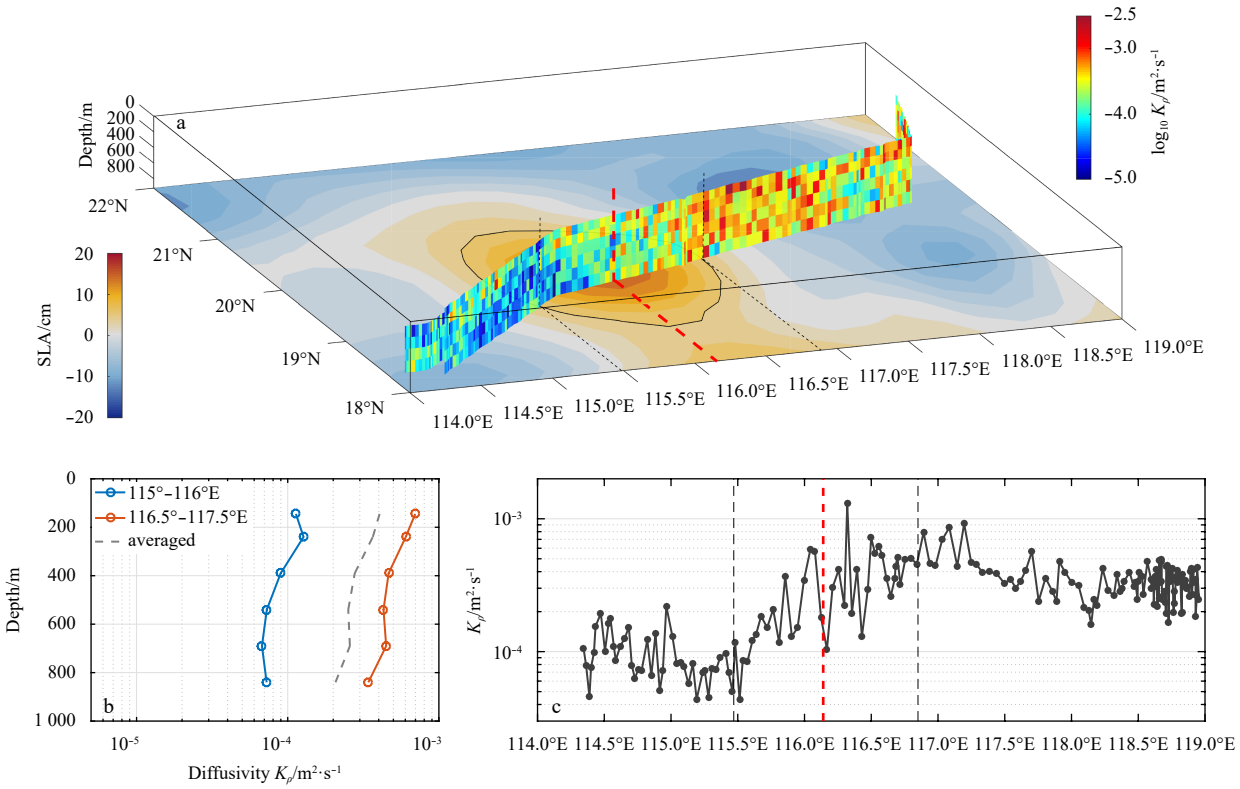

Fig. 5. Estimates of GHP parameterization. a. 3D view of diffusivity, K_ρ, along the glider track. The colors indicate SLA values on May 18, 2015; the black line shows the edge of the anticyclonic eddy, identified following Chelton et al. (2011); and the red dashed line indicates the eddy center. b. Averaged diffusivities by depth related to the eddy anterior side (blue) and posterior side (red). The dashed line indicates the averaged values. c. Variation in diffusivity by longitude. The vertical red and black dashed lines indicate the eddy center and edge, respectively.

values in the order of 10^{-3} m^2/s were observed at the posterior side of the anticyclonic mesoscale eddy. At the anterior side, diffusivity was much weaker, with a maximum of approximately 10^{-4} m^2/s.

To further identify the spatial asymmetry in the eddy diffusivity, the diffusivity profiles were sorted and averaged for the posterior edge side of motion (between 116.5° and 117.7°E) and the anterior side (between 115° and 116°E) (Fig. 5b). The resulting composites show significant differences; the diffusivity at the posterior side of the eddy was approximately seven times higher than at the anterior side, from 100 m to 800 m, the range of which was effectively influenced by the eddy. We also averaged the diffusivity in each profile, and then displayed these averaged diffusivities by longitude (Fig. 5c). The maximum diffusivity was recorded at the posterior edge of the eddy, gradually weakening eastward towards the Luzon Strait and rapidly decreasing southwestward.

Using GHP parameterization and Argo data, Yang et al. (2014) reported that depth-averaged diffusivity values have a linearly decreasing trend southwestwards from the Luzon Strait towards Hainan Island. We obtained a similar result, whereby diffusivity near the Luzon Strait was generally observed to be higher than in the southwest region of the glider track (Fig. 5c). However, due to the influence of the anticyclonic eddy, diffusivity did not show clear linearity as reported by Yang et al. (2014).

3.4.2 *Thorpe-scale results*

An example of an overturn with a depth range from 475 m to 505 m was identified at 19.86°N, 117.031°E in the northern SCS, where the water depth is about 1 800 m (Fig. 6). The potential temperature in the water column was nearly uniform in vertically. The sorted and original potential temperature profiles show an obvious overturn with cooler water overlying warmer water.

Based on the detected overturns, the spatial pattern of diffusivity between 100 m and 800 m is reconstructed by Thorpe-scale estimates (Fig. 7). It shows a small amount of overturns were detected between 115.5° and 118°E, and few overturn existed less than 115.5°E. The disadvantage of the Thorpe-scale method is that overturns could not be easily detected in the upper layer if there exist strong stratifications. As shown in Fig. 7, few overturn was detected in the upper layer where the depth was lesser than 300 m. Abundant overturns were detected where the glider operated near the Luzon Strait (longitude>118°E), which is probably related to active internal waves there. We averaged the diffusivity in each profile, and then displayed these averaged diffusivities by longitude (Fig. 8). Before the averaged diffusivity was obtained, the nonexistent diffusivity in Fig. 7 was assumed to be the background diffusivity of 1×10^{-5} m^2/s. It showed that the diffusivity at the posterior edge was greater than that at the anterior edge.

When comparing the results of GHP scaling (Fig. 5c) and Thorpe-scale method (Fig. 8), it showed some common characteristics. Similar turbulence levels and spatial patterns suggest that elevated diffusivities at the posterior side of the eddy are reliable in this study.

4 Discussion

In the upper ocean, mixing is mainly driven by wind-stress stirring and buoyancy flux (Shay and Gregg, 1986). The action of

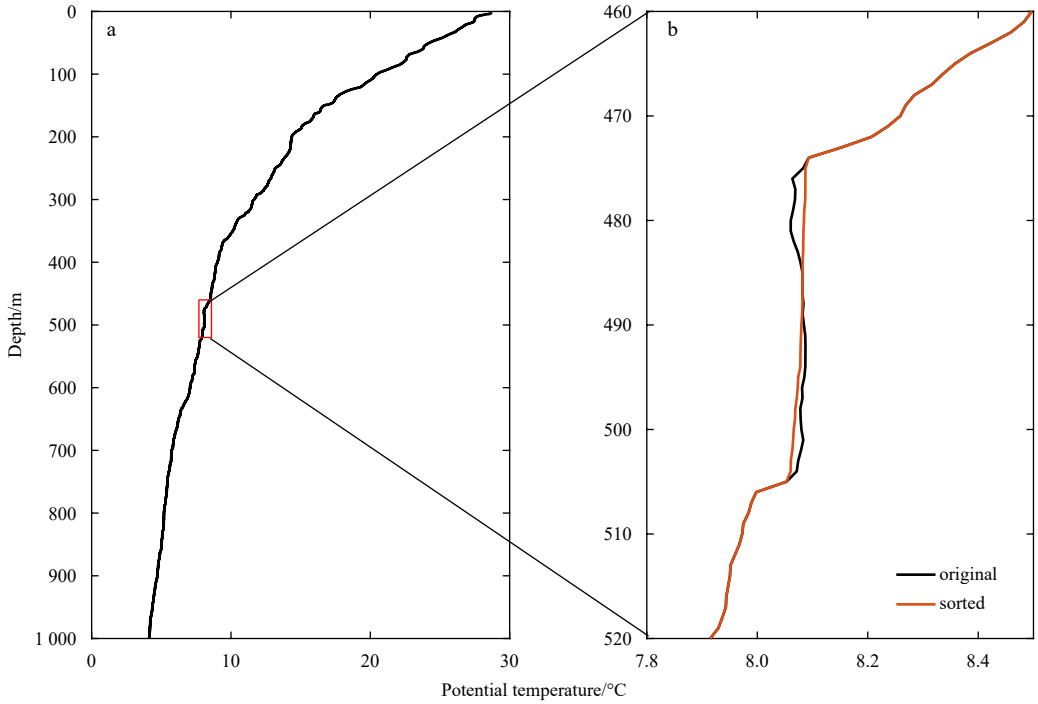

Fig. 6. An example of overturn identified at 19.86°N, 117.031°E in the northern SCS. a. Vertical profiles of potential temperature. b. An overturn detected from the original and sorted potential temperature profiles in the depth range indicated by the orange box in a.

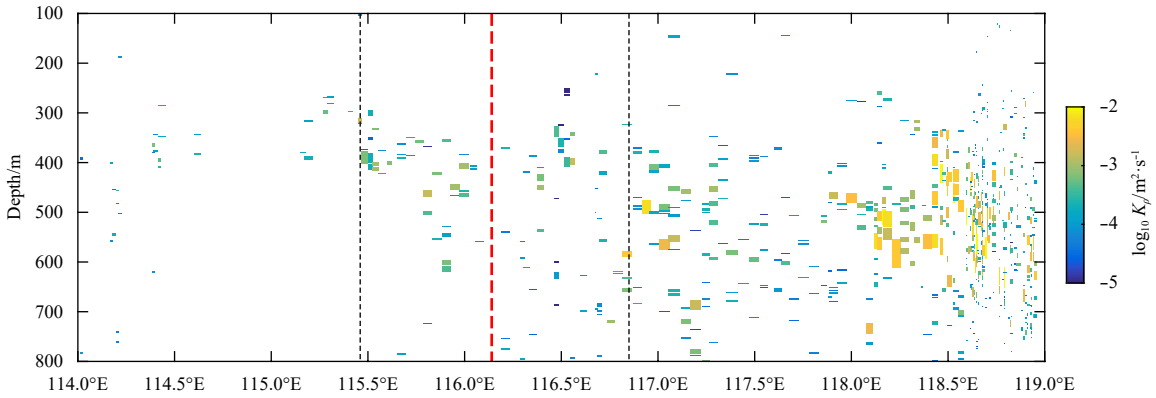

Fig. 7. The spatial pattern of diffusivity reconstructed by Thorpe-scale estimates.

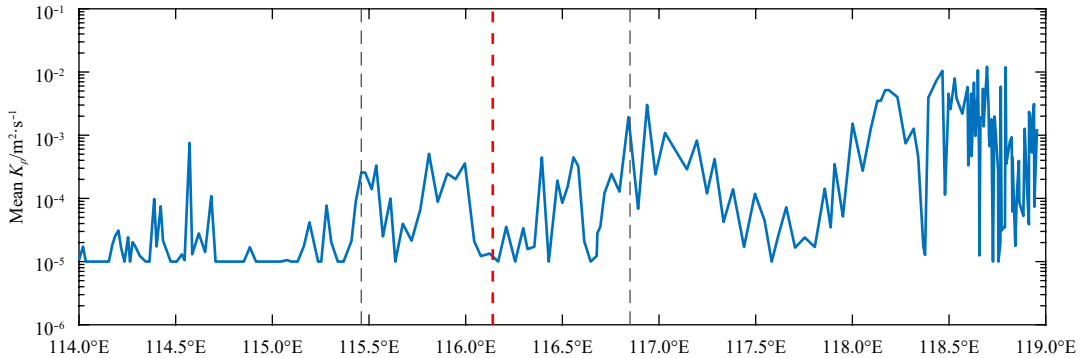

Fig. 8. Variation in diffusivity derived with Thorpe-scale method by longitude. The vertical red and black dashed lines indicate the eddy center and edge, respectively.

Reynolds stress on wind-induced vertical shear is limited to the upper layer (12.5-m depth) under low wind conditions (Callaghan et al., 2014). Furthermore, the effects of buoyancy flux only extend to the bottom of the mixed layer (Shang et al., 2017). In our study, we considered data that were collected below 100 m, and wind speeds were in the range of 1–8 m/s during the observation period. Wind data were obtained from the blended wind dataset (Zhang et al., 2006) and the low wind condition meaning that there is no evidence to suggest that the elevated diffusivities (Fig. 5a) below 100 m resulted from wind stress and buoyancy.

We tracked eddy kinetic energy (EKE) corresponding to the moving path of the anticyclonic mesoscale eddy, and compared this with the bin-averaged diffusivities in relation to longitude (Fig. 9a). Our analysis showed that the diffusivity varied simultaneously with EKE, with the coefficient of determination (R^2) of linear fitting was 0.17. This indicates that the pattern of observed diffusivity was likely caused by the eddy and was related to surface velocity and EKE.

It is known that internal tides provide one of the major dynamical pathways for large-scale energy transfer in the ocean to small-scale turbulent dissipation and mixing. Numerical simulations and observations have confirmed that the Luzon Strait is a multiple generation region of baroclinic internal waves (Zhao et al., 2004; Zhao, 2014; Alford et al., 2015; Wang et al., 2016). After their generation, low-mode internal waves can propagate into the northern SCS. The studied area is a region with active internal waves, the breaking of which may provide a particularly potent energy source for ocean mixing (Gregg et al., 2003). Previous studies have confirmed that, in the South China Sea, the mixing weakens further from Luzon Strait (Wang et al., 2016; Yang et al., 2016). As shown in Figs 5 and 8, diffusivity tended towards larger values close to the Luzon Strait while elevated diffusivities between 116° and 117.5°E did not simply relate to the energy source from internal waves but, rather, to the mesoscale eddy. Numerical simulation and satellite remote sensing observations have confirmed that interactions between internal waves and mesoscale eddies are active in this area (Xie et al., 2015).

It is necessary to understand the dynamic mechanism of the enhanced mixing at the posterior edge side of the anticyclonic eddy (i.e., 116° to 117.5°E). As such, the fine structure shear variances were analyzed using the geostrophic velocities that inferred from the glider data (Fig. 10a), where shear variance was calculated as $S^2=(\partial u/\partial z)^2+(\partial v/\partial z)^2$. It is shown that elevated shear variance was found in the region effected by the anticyclonic eddy, with the maximum shear variance in the depth of about 100 m (Fig. 10a). We also compared shear variance among three regions, namely the posterior edge side (between 116.8° and 117.2°E), the anterior edge side (between 114.8° and 115.2°E), and the peripheral region (between 118° and 118.4°E). The maximum S^2 values at the posterior edge side reached 3×10^{-6} s^{-2}, which was larger than at the anterior and peripheral regions (Fig. 10b). Furthermore, the S^2 values at the posterior edge were larger than at the other two regions throughout water column. Higher shear variance at the posterior side, which is prone to triggering shear instabilities, may be the main mechanism for the corresponding elevated diffusivity.

The surface currents at the posterior edge region of the eddy were larger than the other two regions (Fig. 9b). In some cases, the velocity at the base of the eddy was distinct or even showed the opposite trend to that within the eddy, whereby strengthened shear can be generated in areas of stronger surface currents (Liang and Thurnherr, 2011; Zhang et al., 2014). The higher shears at the posterior side can also be caused by the eddy tilt. Because the eddy propagation in the northern SCS follows the regional sloping bottom topography, the topographic β effect, which exerts more influence to the water column near bottom in the stratified ocean is likely the cause for the observed vertically tilting structures (Zhang et al., 2016). As shown in Fig. 4d, the westward tilt of eddy reached 0.3° of longitude from surface to lower layer of 1 000 m, which mean the higher shears at the posterior side were partly contributed by the eddy tilt, and the background velocity field. The higher shear at the posterior side may have led to the breaking of internal waves, which could have caused the relatively high diffusivity values in the thermocline. Alternatively, internal waves may become trapped by higher shear at the posterior side of eddies, thereby transferring momentum to the deeper ocean and facilitating mixing (Booker and Bretherton, 1967; Zhang et al., 2014).

Sub-mesoscale motion is a common physical process in the ocean and plays an important role in energy cascades from large-scale to small-scale motion (Fu and Ferrari, 2008; Chelton et al., 2011). In Fig. 3d, two velocity cores with maximum absolute geostrophic velocity values (approximately 0.8 m/s) were found at the edges of the eddy. In some case, strong turbulent mixing is found in the edge of the eddy and is controlled by the geostrophic velocity generated shear (Liu et al., 2017). Also, with such high velocities, a strong horizontal shear generates instability and favors sub-mesoscale eddy formation (Capet et al., 2008; Thomas and Ferrari, 2008). Sub-mesoscale motion has been previously reported at the posterior edge of anticyclonic eddies. For example, Qiu et al. (2019a) analyzed drifter buoy data and found clear signals of sub-mesoscale motion at the posterior edge of an anticyclonic eddy in the northern SCS but not at the anterior edge.

Mesoscale eddies can feed the generation and growth of sub-mesoscale motions. For example, Zhang et al. (2016) reported the dynamical process of sub-mesoscale motion accounts for more than 50% of the dissipation processes of anticyclonic eddies in the northern SCS. In our study, sub-mesoscale signals could be seen in the density anomalies (Fig. 11), which exhibited significant oscillations. This spatial variability may be caused by ocean convection or other sub-mesoscale structures (Su et al., 2016; Qiu et al., 2019a). As shown in Fig. 11, the density anomaly at the posterior edge of the eddy had more significant oscillations than at the anterior edge. Here the density anomaly is calculated as $\rho'=\rho-\rho_b(z)$, where $\rho_b(z)$ is a depth-dependent background density defined as horizontal mean over the interested domain between 114.5° and 118°E. In order to better validate the existence of sub-mesoscale motions with the glider data, a 50 km high-pass filter is used to process the density anomaly data in each layer of depth to eliminating the effects of larger scale fluctuations. Then we calculate the longitude-dependent standard deviation (std) of the high-passing data between the depth of 60 m and 300 m (Fig. 12) for each profile, for the vertical area affected by studied mesoscale eddy was mainly concentrated in that depth. It is supposed that the std of density anomaly can validate the richness of sub-mesoscale motion to some extent. Although the high-pass-filtered data may include the information on internal waves and tides, the variation of std of density anomaly at the order of killometers caused by internal waves and tides is possibly not significant. In Fig. 12, it shows the std of density anomaly at the posterior edge was higher than that at the anterior edge, which indicated that the features of sub-mesoscale motions were more abundant there. It should be noted that the energy cascade from mesoscale to sub-mesoscale eddies cannot be

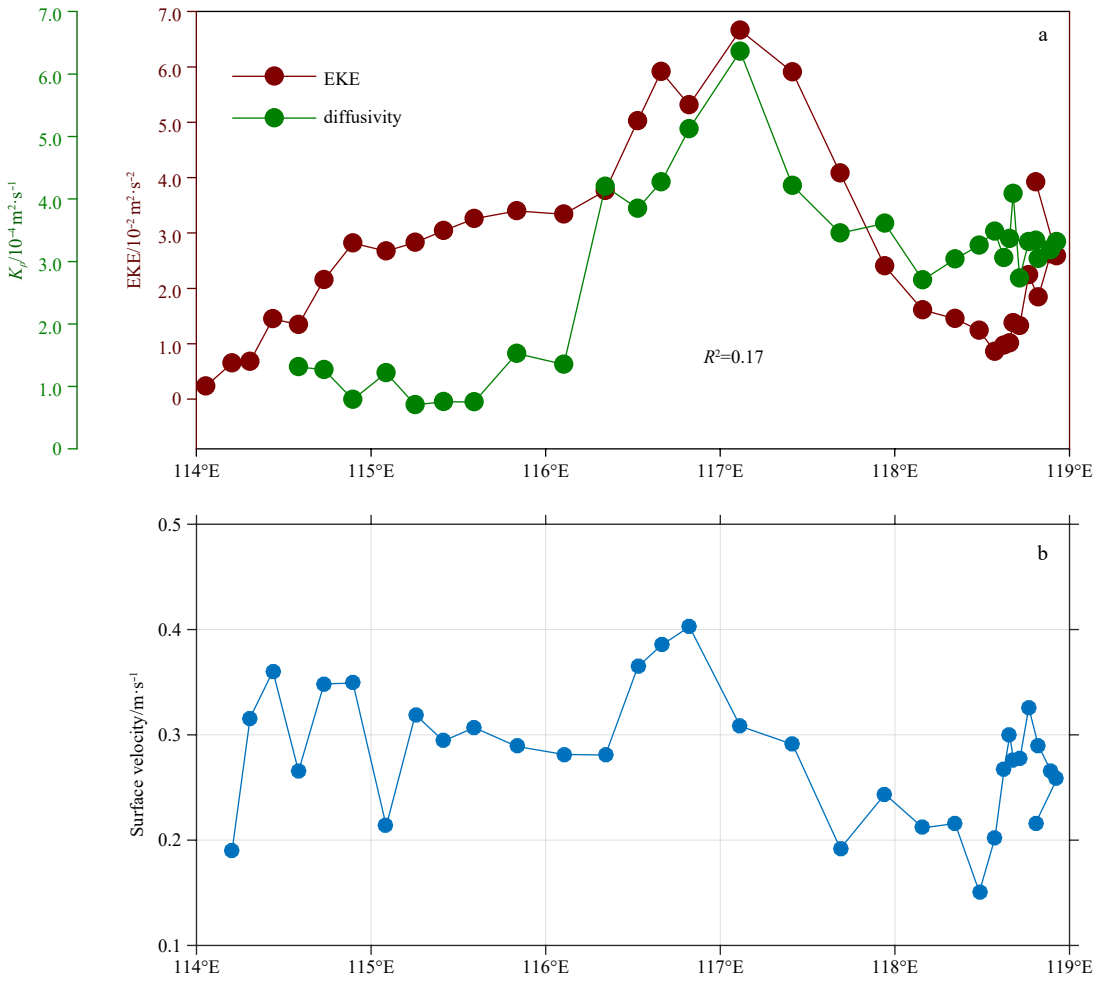

Fig. 9. Comparison of eddy kinetic energy, diffusivity, and surface velocity. a. Eddy kinetic energy (EKE) corresponding to the moving path of the studied anticyclonic mesoscale eddy and the bin-averaged diffusivities by longitude. R^2 is the linear fitting coefficient of determination. b. Bin-averaged surface velocity by longitude. The velocity was derived from HYCOM.

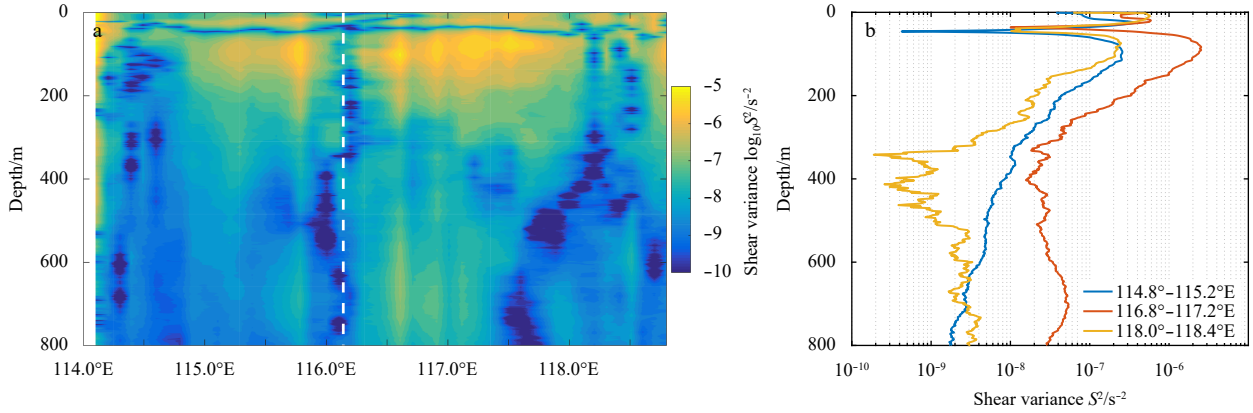

Fig. 10. Fine structure shear variances derived from geostrophic velocities. a. Section display. b. Averaged shear variance in the posterior edge region (red), anterior edge region (blue), and the peripheral region (yellow).

accounted for by GHP parameterization based on the wave-wave interaction theory but can be accounted for by Thorpe-scale method. As the results from the Thorpe-scale method shown in Fig. 8, the mixing at the posterior edge was enhanced, which indicated the effect of sub-mesoscale on the enhancement of vertical mixing. Based on these observations, it is reasonable to suggest that downward energy transfer to sub-mesoscale motion plays an important role in the dissipation of oceanic eddies, which may be a common phenomenon in the ocean.

5 Summary

In this study, we estimated the spatial structure of turbulent

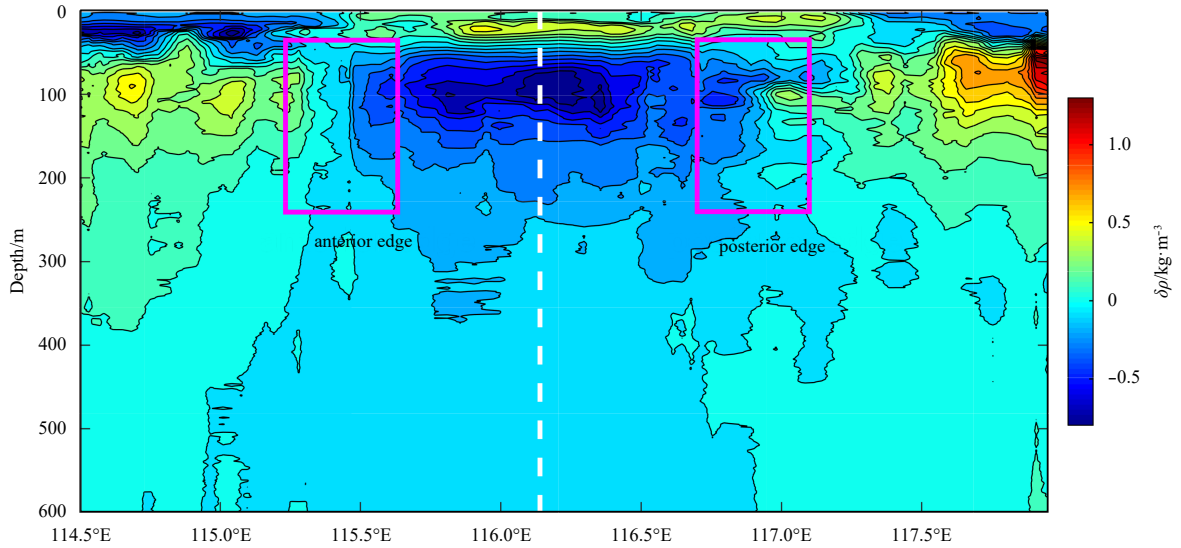

Fig. 11. Contour map of density anomalies $\delta\rho$. The white line shows the core of the eddy. The anterior and posterior edges are marked with pink boxes.

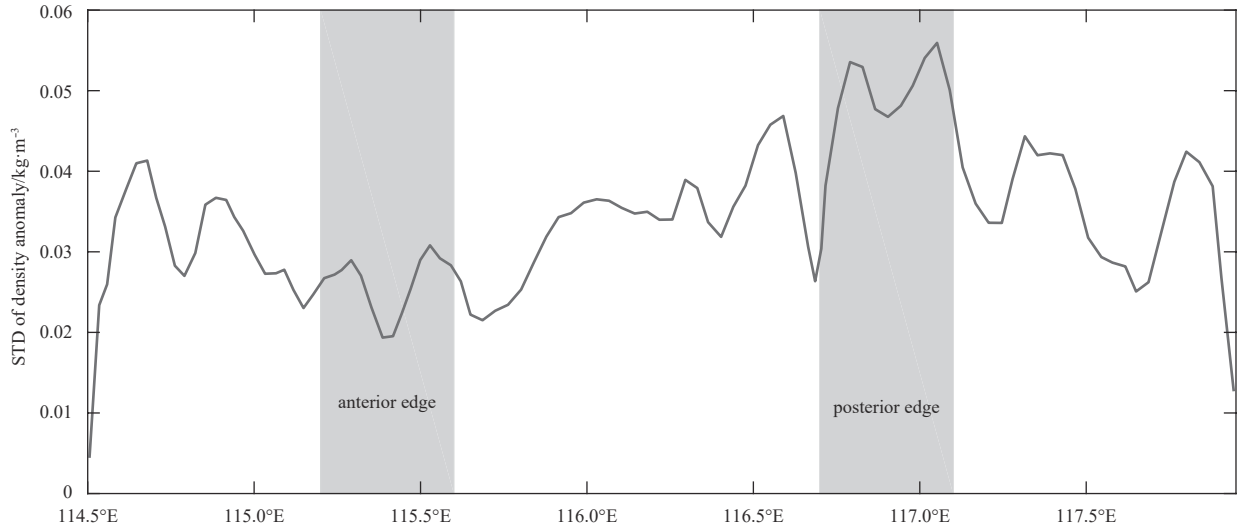

Fig. 12. Longitude-dependent standard deviation of the density anomaly between 60 m and 300 m.

mixing of an anticyclonic eddy in the northern SCS from underwater glider data (May 2015) using the Gregg-Henyey-Polzin parameterization and the Thorpe-scale method. Highly enhanced diffusivity rates on the order of 10^{-3} m^2/s were found at the posterior edge of the studied anticyclonic eddy. In the anterior edge region, diffusivity was one order of magnitude lower, consistent with the previously reported background values for turbulent mixing in the north SCS (Zhang et al., 2016; Shang et al., 2017). Potential mechanisms for these high diffusivity values include the effects of higher background vertical shear variance due to the anticyclonic eddy, internal waves trapped by shear, and sub-mesoscale motion fed by the mesoscale eddy.

In summary, the diffusivity data were highly asymmetrical in the mesoscale eddy area with a non-uniform horizontal and vertical structure. Although mixing processes in the northern SCS have been widely studied, the previous work has focused on large scale data with resolutions that greater than dozens of kilometers (Tian et al., 2009; Liang et al., 2017). Here, we identified mixing patterns based on a spatial resolution of approximately 4 km that was able to characterize sub-mesoscale motion. We believe that the observed mixing patterns of high spatial resolutions within the anticyclonic eddy will help to improve our knowledge of the turbulent mixing process in the northern SCS.

Acknowledgements

The Chinese underwater glider was provided by the State Key Laboratory of Robotics, Shenyang Institute of Automation. We acknowledge CMEMS for sea-level anomaly data, HYCOM for surface velocity data, the Aviso eddy atlas for physical field data, the Blended sea wind dataset for sea-surface wind data, and the Argo dataset for historical temperature and salinity data. The numerical simulation is supported by High Performance Computing Division and HPC managers of Wei Zhou and Dandan Sui from the South China Sea Institute of Oceanology.

References

Alford M H, Peacock T, Mackinnon J M, et al. 2015. The formation and fate of internal waves in the South China Sea. Nature, 521(7550): 65–69, doi: 10.1038/nature14399

Bai Xiaolin, Liu Zhiyu, Zheng Quanan, et al. 2019. Fission of shoaling internal waves on the northeastern shelf of the South China Sea. Journal of Geophysical Research: Oceans, 124(7): 4529–4545, doi: 10.1029/2018JC014437

Booker J R, Bretherton F P. 1967. The critical layer for internal gravity waves in a shear flow. Journal of Fluid Mechanics, 27(3): 513–539, doi: 10.1017/S0022112067000515

Callaghan A H, Ward B, Vialard J. 2014. Influence of surface forcing on near-surface and mixing layer turbulence in the tropical Indian Ocean. Deep Sea Research Part I: Oceanographic Research Papers, 94: 107–123, doi: 10.1016/j.dsr.2014.08.009

Capet X, McWilliams J, Molemaker M, et al. 2008. Mesoscale to submesoscale transition in the California current system. Part I: Flow structure, eddy flux, and observational tests. Journal of Physical Oceanography, 38(1): 29–43, doi: 10.1175/2007JPO3671.1

Caruso M J, Gawarkiewicz G G, Beardsley R C. 2006. Interannual variability of the Kuroshio intrusion in the South China Sea. Journal of Oceanography, 62(4): 559–575, doi: 10.1007/s10872-006-0076-0

Chelton D B, Schlax M G, Samelson R M. 2011. Global observations of nonlinear mesoscale eddies. Progress in Oceanography, 91(2): 167–216, doi: 10.1016/j.pocean.2011.01.002

Chen Gengxin, Hou Yijun, Chu Xiaoqing. 2011. Mesoscale eddies in the South China Sea: Mean properties, spatiotemporal variability, and impact on thermohaline structure. Journal of Geophysical Research: Ocean, 116(C6): C06018

Chow C H, Hu J H, Centurioni L R, et al. 2008. Mesoscale Dongsha cyclonic eddy in the northern South China Sea by drifter and satellite observations. Journal of Geophysical Research: Ocean, 113(C4): C04018, doi: 10.1029/2007JC004542

Chu Xiaoqing, Xue Huijie, Qi Yiquan, et al. 2014. An exceptional anticyclonic eddy in the South China Sea in 2010. Journal of Geophysical Research: Oceans, 119(2): 881–897, doi: 10.1002/2013JC009314

Dillon T M. 1982. Vertical overturns: A comparison of Thorpe and Ozmidov length scales. Journal of Geophysical Research: Oceans, 87(C12): 9601–9613, doi: 10.1029/JC087iC12p09601

Ferrari R, Wunsch C. 2009. Ocean circulation kinetic energy: Reservoirs, sources, and sinks. Annual Review of Fluid Mechanics, 41: 253–282, doi: 10.1146/annurev.fluid.40.111406.102139

Fu L L, Ferrari R. 2008. Observing oceanic submesoscale processes from space. Eos, Transactions, American Geophysical Union, 89(48): 488, doi: 10.1029/2008EO480003

Garrett C, Munk W. 1972. Space-time scales of internal waves. Geophysical Fluid Dynamic, 3(3): 225–264, doi: 10.1080/03091927208236082

Garrett C, Munk W. 1975. Space-time scales of internal waves: A progress report. Journal of Geophysical Research, 80(3): 291–297, doi: 10.1029/JC080i003p00291

Gill A E, Green J S A, Simmons A J. 1974. Energy partition in the large-scale ocean circulation and the production of mid-ocean eddies. Deep Sea Research and Oceanographic Abstracts, 21(7): 499–528, doi: 10.1016/0011-7471(74)90010-2

Gregg M C, Sanford T B, Winkel D P. 2003. Reduced mixing from the breaking of internal waves in equatorial waters. Nature, 422(6931): 513–515, doi: 10.1038/nature01507

Guo Jingsong, Feng Ying, Yuan Yeli, et al. 2013. Kuroshio loop current intruding into the South China Sea and its shedding eddy. Oceanologia et Limnologia Sinica (in Chinese), 44(3): 537–544

He Qingyou, Zhan Haigang, Cai Shuqun, et al. 2018. A new assessment of mesoscale eddies in the South China Sea: Surface features, three-dimensional structures, and thermohaline transports. Journal of Geophysical Research: Oceans, 123(7): 4906–4929, doi: 10.1029/2018JC014054

Henyey F S, Wright J, Flatté S M. 1986. Energy and action flow through the internal wave field: An eikonal approach. Journal of Geophysical Research: Oceans, 91(C7): 8487–8495, doi: 10.1029/JC091iC07p08487

Hu Jianyu, Zheng Quanan, Sun Zhenyu, et al. 2012. Penetration of nonlinear Rossby eddies into South China Sea evidenced by cruise data. Journal Geophysical Research: Oceans, 117(C3): C03010

Huang Xiaodong, Chen Zhaohui, Zhao Wei, et al. 2016. An extreme internal solitary wave event observed in the northern South China Sea. Scientific Reports, 6: 30041, doi: 10.1038/srep30041

Jia Yinglai, Chassignet E P. 2011. Seasonal variation of eddy shedding from the Kuroshio intrusion in the Luzon Strait. Journal of Oceanography, 67(5): 601–611, doi: 10.1007/s10872-011-0060-1

Jia Yinglai, Liu Qinyu, Liu Wei. 2004. Eddy shedding from the Kuroshio bend at Luzon Strait. Journal of Oceanography, 60(6): 1063–1069, doi: 10.1007/s10872-005-0014-6

Jing Zhao, Wu Lixin. 2013. Low-frequency modulation of turbulent diapycnal mixing by anticyclonic eddies inferred from the HOT time series. Journal of Physical Oceanography, 43(3): 824–835

Klymak J M, Alford M H, Pinkel R, et al. 2011. The breaking and scattering of the internal tide on a continental slope. Journal of Physical Oceanography, 41(5): 926–945, doi: 10.1175/2010JPO4500.1

Kunze E, Firing E, Hummon J M, et al. 2006. Global abyssal mixing inferred from lowered ADCP shear and CTD strain profiles. Journal of Physical Oceanography, 36(8): 1553–1576, doi: 10.1175/JPO2926.1

Li Li, Nowlin W D Jr, Su Jilan. 1998. Anticyclonic rings from the Kuroshio in the South China Sea. Deep Sea Research Part I: Oceanographic Research Papers, 45(9): 1469–1482, doi: 10.1016/S0967-0637(98)00026-0

Li Li, Pohlmann T. 2002. The South China Sea warm-core ring 94S and its influence on the distribution of chemical tracers. Ocean Dynamics, 52(3): 116–122, doi: 10.1007/s10236-001-0009-9

Liang Changrong, Chen Guiying, Shang Xiaodong. 2017. Observations of the turbulent kinetic energy dissipation rate in the upper central South China Sea. Ocean Dynamics, 67(5): 597–609, doi: 10.1007/s10236-017-1051-6

Liang Xinfeng, Thurnherr A M. 2011. Subinertial variability in the deep ocean near the East Pacific Rise between 9° and 10°N. Geophysical Research Letters, 38(6): L06606

Liu Zhiyu, Lian Qiang, Zhang Fangtao, et al. 2017. Weak thermocline mixing in the North Pacific low-latitude western boundary current system. Geophysical Research Letters, 44(20): 10530–10539, doi: 10.1002/2017GL075210

Mater B D, Venayagamoorthy S K, St Laurent L, et al. 2015. Biases in Thorpe-scale estimates of turbulence dissipation. Part I: Assessments from large-scale overturns in oceanographic data. Journal of Physical Oceanography, 45(10): 2497–2521, doi: 10.1175/JPO-D-14-0128.1

Nan Feng, Xue Huijie, Chai Fei, et al. 2011a. Identification of different types of Kuroshio intrusion into the South China Sea. Ocean Dynamics, 61(9): 1291–1304, doi: 10.1007/s10236-011-0426-3

Nan Feng, Xue Huijie, Xiu Peng, et al. 2011b. Oceanic eddy formation and propagation southwest of Taiwan. Journal of Geophysical Research: Oceans, 116(C12): C12045, doi: 10.1029/2011JC007386

Nan Feng, Xue Huijie, Yu Fei. 2015. Kuroshio intrusion into the South China Sea: A review. Progress in Oceanography, 137: 314–333, doi: 10.1016/j.pocean.2014.05.012

Osborn T R. 1980. Estimates of the local rate of vertical diffusion from dissipation measurements. Journal of Oceanography, 10(1): 83–89

Park J H, Farmer D. 2013. Effects of Kuroshio intrusions on nonlinear internal waves in the South China Sea during winter. Journal of Geophysical Research: Oceans, 118(12): 7081–7094, doi: 10.1002/2013JC008983

Polzin K L, Garabato A C N, Huussen T N, et al. 2014. Finescale parameterizations of turbulent dissipation. Journal of Geophysical Research: Oceans, 119(2): 1383–1419, doi: 10.1002/2013JC008979

Qiu Chunhua, Mao Huabin, Liu Hailong, et al. 2019a. Deformation of a warm eddy in the northern South China Sea. Journal of Geophysical Research: Oceans, 124(8): 5551–5564, doi: 10.1029/2019JC015288

Qiu Chunhua, Mao Huabin, Wang Yanhui, et al. 2019b. An irregularly shaped warm eddy observed by Chinese underwater gliders. Journal of Oceanography, 75(2): 139–148, doi: 10.1007/s10872-018-0490-0

Qu Tangdong. 2000. Upper-layer circulation in the South China Sea. Journal of Physical Oceanography, 30(6): 1450–1460, doi: 10.1175/1520-0485(2000)030<1450:ULCITS>2.0.CO;2

Qu Tangdong, Girton J B, Whitehead J A. 2006. Deepwater overflow through Luzon Strait. Journal of Geophysical Research: Oceans, 111(C1): C01002

Shang Xiaodong, Liang Changrong, Chen Guiying. 2017. Spatial distribution of turbulent mixing in the upper ocean of the South China Sea. Ocean Science, 13(3): 503–519, doi: 10.5194/os-13-503-2017

Shay T J, Gregg M C. 1986. Convectively driven turbulent mixing in the upper ocean. Journal of Physical Oceanography, 16(11): 1777–1798, doi: 10.1175/1520-0485(1986)016<1777:CDTMIT>2.0.CO;2

St. Laurent L 2008. Turbulent dissipation on the margins of the South China Sea. Geophysical Research Letters, 35(23): L23615, doi: 10.1029/2008GL035520

Su Zhan, Ingersoll A P, Stewart A, et al. 2016. Ocean convective available potential energy. Part II: Energetics of thermobaric convection and thermobaric cabbeling. Journal of the Physical Oceanography, 46(4): 1097–1115, doi: 10.1175/JPO-D-14-0156.1

Sun Hui, Yang Qingxuan, Zhao Wei, et al. 2016. Temporal variability of diapycnal mixing in the northern South China Sea. Journal of Geophysical Research: Oceans, 121(12): 8840–8848, doi: 10.1002/2016JC012044

Thomas L, Ferrari R. 2008. Friction, frontogenesis, and the stratification of the surface mixed layer. Journal of Physical Oceanography, 38(11): 2501–2518, doi: 10.1175/2008JPO3797.1

Tian Jiwei, Yang Qingxuan, Zhao Wei. 2009. Enhanced diapycnal mixing in the South China Sea. Journal of Physical Oceanography, 39(12): 3191–3203, doi: 10.1175/2009JPO3899.1

Wang Xiaowei, Peng Shiqiu, Liu Zhiyu, et al. 2016. Tidal mixing in the South China Sea: An estimate based on the internal tide energetics. Journal of Physical Oceanography, 46(1): 107–124, doi: 10.1175/JPO-D-15-0082.1

Wang Guihua, Su Jilan, Chu P C. 2003. Mesoscale eddies in the South China Sea observed with altimeter data. Geophysical Research Letters, 30(21): 2121, doi: 10.1029/2003GL018532

Wang Guihua, Su Jilan, Qi Yiquan. 2005. Advances in studying mesoscale eddies in South China Sea. Advance in Earth Science, 20(8): 882–886

Wang Guihua, Xie Shangping, Qu Tangdong, et al. 2011. Deep South China Sea circulation. Geophysical Research Letters, 38(5): L05601

Wang Dongxiao, Xu Hongzhou, Lin Jing, et al. 2008. Anticyclonic eddies in the northeastern South China Sea during winter 2003/2004. Journal of Oceanography, 64(6): 925–935, doi: 10.1007/s10872-008-0076-3

Wang Qiang, Zeng Lili, Li Jian, et al. 2018. Observed cross-shelf flow induced by mesoscale eddies in the northern South China Sea. Journal of Physical Oceanography, 48(7): 1609–1628, doi: 10.1175/JPO-D-17-0180.1

Xie Jieshuo, He Yinghui, Chen Zhiwu, et al. 2015. Simulations of internal solitary wave interactions with mesoscale eddies in the northeastern South China Sea. Journal of Physical Oceanography, 45(12): 2959–2978, doi: 10.1175/JPO-D-15-0029.1

Xie Shangping, Xie Qiang, Wang Dongxiao, et al. 2003. Summer upwelling in the South China Sea and its role in regional climate variations. Journal of Geophysical Research: Oceans, 108(C8): 3261, doi: 10.1029/2003JC001867

Yang Haijun, Liu Qinyu. 2003. Forced Rossby wave in the northern South China Sea. Deep Sea Research Part I: Oceanographic Research Papers, 50(7): 917–926, doi: 10.1016/S0967-0637(03)00074-8

Yang Qingxuan, Nikurashin M, Sasaki H, et al. 2019. Dissipation of mesoscale eddies and its contribution to mixing in the northern South China Sea. Scientific Reports, 9: 556, doi: 10.1038/s41598-018-36610-x

Yang Qingxuan, Zhou Lei, Tian Jiwei, et al. 2014. The roles of Kuroshio intrusion and mesoscale eddy in upper mixing in the northern South China Sea. Journal of Coastal Research, 30(1): 192–198

Yang Qingxuan, Zhao Wei, Liang Xinfeng, et al. 2016. Three-dimensional distribution of turbulent mixing in the South China Sea. Journal of Physical Oceanography, 46(3): 769–788, doi: 10.1175/JPO-D-14-0220.1

Yang Qingxuan, Zhao Wei, Liang Xinfeng, et al. 2017. Elevated mixing in the periphery of mesoscale eddies in the South China Sea. Journal of Physical Oceanography, 47(4): 895–907, doi: 10.1175/JPO-D-16-0256.1

Yuan Dongliang, Han Weiqing, Hu Dunxin. 2006. Surface Kuroshio path in the Luzon Strait area derived from satellite remote sensing data. Journal of Geophysical Research: Oceans, 111(C11): C11007, doi: 10.1029/2005JC003412

Yuan Dongliang, Han Weiqing, Hu Dunxin. 2007. Anti-cyclonic eddies northwest of Luzon in summer-fall observed by satellite altimeters. Geophysical Research Letters, 34(13): L13610

Zhang Huaimin, Bates J J, Reynolds R W. 2006. Assessment of composite global sampling: Sea surface wind speed. Geophysical Research Letters, 33(17): L17714, doi: 10.1029/2006GL027086

Zhang Zhiwei, Tian Jiwei, Qiu Bo, et al. 2016. Observed 3D structure, generation, and dissipation of oceanic mesoscale eddies in the South China Sea. Scientific Reports, 6: 24349, doi: 10.1038/srep24349

Zhang Zhengguang, Wang Wei, Qiu Bo. 2014. Oceanic mass transport by mesoscale eddies. Science, 345(6194): 322–324, doi: 10.1126/science.1252418

Zhang Zhiwei, Zhao Wei, Qiu Bo, et al. 2017. Anticyclonic eddy sheddings from Kuroshio loop and the accompanying cyclonic eddy in the northeastern South China Sea. Journal Physical Oceanography, 47(6): 1243–1259, doi: 10.1175/JPO-D-16-0185.1

Zhang Zhiwei, Zhao Wei, Tian Jiwei, et al. 2013. A mesoscale eddy pair southwest of Taiwan and its influence on deep circulation. Journal Geophysical Research: Oceans, 118(12): 6479–6494, doi: 10.1002/2013JC008994

Zhao Zhongxiang. 2014. Internal tide radiation from the Luzon Strait. Journal of Geophysical Research: Ocean, 119(8): 5434–5448, doi: 10.1002/2014JC010014

Zhao Zhongxiang, Klemas V, Zheng Quanan, et al. 2004. Remote sensing evidence for baroclinic tide origin of internal solitary waves in the northeastern South China Sea. Geophysical Research Letters, 31(6): L06302

Zheng Quanan, Xie Lingling, Zheng Zhiwen, et al. 2017. Progress in research of mesoscale eddies in the South China Sea. Advances in Marine Science, 35(2): 131–158

Zhou Chun, Zhao Wei, Tian Jiwei, et al. 2014. Variability of the deep-water overflow in the Luzon Strait. Journal of Physical Oceanography, 44(11): 2972–2986, doi: 10.1175/JPO-D-14-0113.1